Pharm Res (2014) 31:305–321
DOI 10.1007/s11095-013-1161-x

RESEARCH PAPER

The Importance of Villous Physiology and Morphology in Mechanistic Physiologically-Based Pharmacokinetic Models

Emile P. Chen • Guoying Tai • Harma Ellens

Received: 17 April 2013 / Accepted: 28 July 2013 / Published online: 30 August 2013

ABSTRACT

Purpose Existing PBPK models incorporating intestinal first-pass metabolism account for effect of drug permeability on accessible absorption surface area by use of "effective" permeability, P_{eff}, without adjusting number of enterocytes involved in absorption or proportion of intestinal CYP3A involved in metabolism. The current model expands on existing models by accounting for these factors.

Methods The PBPK model was developed using SAAM II. Midazolam clinical data was generated at GlaxoSmithKline.

Results The model simultaneously captures human midazolam blood concentration profile and previously reported intestinal availability, using values for CYP3A CLu_{int}, permeability and accessible surface area comparable to literature data. Simulations show: (1) failure to distinguish absorbing from non-absorbing enterocytes results in overestimation of intestinal metabolism of highly permeable drugs absorbed across the top portion of the villous surface only; (2) first-pass extraction of poorly permeable drugs occurs primarily in enterocytes, drugs with higher permeability are extracted by enterocytes and hepatocytes; (3) CYP3A distribution along crypt-villous axes does not significantly impact intestinal metabolism; (4) differences in permeability of perpetrator and victim drugs results in their spatial separation along the villous axis and intestinal length, diminishing drug-drug interaction magnitude.

Conclusions The model provides a useful tool to interrogate intestinal absorption/metabolism of candidate drugs.

KEY WORDS drug-drug interaction · enterocyte · first pass extraction · intestinal availability · intestinal villous

ABBREVIATIONS

AUC	area under the curve
CL	clearance
F	oral bioavailability
F_g	intestinal availability
F_h	hepatic availability
f_{ub}	free fraction in blood
f_{ue}	free fraction in enterocyte
f_{uh}	free fraction in hepatocyte
HLQ	higher limit of quantitation
ICRP	the International Commission on Radiological Protection
LC/MS/MS	high performance liquid chromatography with tandem mass spectrometry
LLQ	lower limit of quantitation
PBPK	physiologically-based pharmacokinetics model
P_{eff}	effective permeability
P-gp	P-glycoprotein

INTRODUCTION

Since a substantial number of marketed drugs are cleared *via* metabolism by Cytochrome P450 3A (CYP3A) (1), it is important during drug discovery and development to be able to estimate the magnitude of first pass extraction by this enzyme and to evaluate the potential for CYP3A drug-drug interactions (DDIs). Static mathematical models are used routinely to interpret *in vitro* data, but do not account for changes in drug concentrations with time and tend to over-predict risk (2). Physiologically based pharmacokinetic models incorporating a sufficient level of anatomical and physiological detail have

E. P. Chen • G. Tai • H. Ellens
Department of Preclinical Drug Metabolism and Pharmacokinetics
GlaxoSmithKline, King of Prussia, Pennsylvania 19406, USA

E. P. Chen (✉)
GlaxoSmithKline, 709 Swedeland Rd. UW2720,
King of Prussia, Pennsylvania 19473, USA
e-mail: emile.p.chen@gsk.com

the potential for better predictions due to their dynamic nature (3).

While the contribution of intestinal CYP3A metabolism to systemic clearance is low, due to the low intestinal enzyme abundance (4,5), it has been shown to contribute significantly to intestinal first-pass metabolism (6,7). Several mathematical models have been developed to explain this apparent discrepancy, incorporating physiological and anatomical details such as (1) separate blood flow to the enterocyte layer from that perfusing the rest of the gut tissues; (2) regional differences in enzyme expression, and (3) permeation-limitations in enterocyte pharmacokinetics (7–10).

The morphology and physiology of the intestinal villous also play an important role in drug absorption. Many investigators have suggested that the villous surface area is not accessible to all drugs equally. Absorption of highly permeable drugs takes place mainly in the upper regions of the villi, since rapid permeation at protruding villous tips reduces the availability of drug for movement into the inter-villous space, whereas poorly permeable drugs have greater opportunity to do so (11,12). The permeability-dependent villous surface accessibility is implicitly accounted for in existing PBPK models by the use of the "effective" permeability term, derived from the *in vitro* permeability (5). Alternatively, the extent by which a compound's passive permeability enables it to diffuse into the inter-villous space has been derived theoretically (13). This theoretical approach has been utilized in SIMCYP's virtual dog model, since the relationship between "effective" and *in-vitro* permeability in the dog is not known.

It is important to note that partial accessibility of the villous surface by higher permeability drugs means absorption of these drugs must involve a reduced set of enterocytes, with a concomitant reduction in villous CYP3A engaged in metabolism. These factors can potentially influence intracellular free drug concentrations and intestinal first-pass extraction. This necessitates the introduction of distinct absorbing and non-absorbing enterocyte compartments at the villous tip and base, respectively. Such treatment also enables consideration of a CYP3A gradient along the crypt-villous axis. Knowledge derived from such a model will not only enhance our understanding of absorption and metabolism of midazolam and other CYP3A substrates, but will also provide a scientific basis for future incorporation of intestinal uptake and efflux transporters to investigate enzyme-transporter interplay in the intestine.

MATERIALS AND METHODS

Data Source

The model developed in the present work was optimized to simultaneously account for the midazolam blood concentration profile and intestinal availability (F_g), which represents the fraction of absorbed drug escaping intestinal first-pass metabolism.

The midazolam plasma concentration data used in the present work is from clinical studies evaluating the drug-drug interaction potential of a GSK development compound. Midazolam blood concentration data used in model evaluation was derived from plasma concentrations by multiplying plasma concentrations by a blood to plasma partitioning ratio of 0.6, which was determined *ex vivo* (14). The studies were performed in healthy postmenopausal female subjects (37–68 years old, mean 57 years, body weight 54–95 kg, mean 69 kg, $N=82$). These studies were open-label, two-period and randomized with respect to dose of the investigational drug. Data from the control sessions where the subjects received midazolam alone were used for the current model development. Each subject received 5 mg of midazolam following an overnight fast for at least 8 h prior to dosing. Blood samples for pharmacokinetic analysis were collected into ethylene diamine tetra-acetic acid (EDTA) tubes on ice/water prior to dosing of midazolam (0 h), and at 0.25, 0.5, 1, 2, 4, 8, 12 and 24 h post-dose. Blood samples were capped, mixed by inversion, then centrifuged at 4°C and 3,000 rpm for 15 min within 1 h of collection and the resultant plasma transferred into 1.8 mL polypropylene Nunc screw capped tubes. Samples were stored frozen at -20°C or colder. Plasma midazolam concentrations were determined using high performance liquid chromatography with tandem mass spectrometry (LC/MS/MS). The lower limit of quantification (LLQ) was 0.5 ng/mL, using a 50 μL aliquot of human plasma with a higher limit of quantification (HLQ) of 100 ng/mL. The human biological samples were sourced ethically and their research use was in accord with the terms of the informed consents.

The fraction of absorbed drug escaping intestinal first-pass extraction ($F_g = 1 - E_g$) of 0.57 ± 0.24 was derived from the intestinal extraction ratio (E_g) of 0.43 ± 0.24 estimated by Thummel *et al.* (15). According to the principle of error propagation F_g and E_g have identical standard deviation.

Pharmacokinetic Analysis

The pharmacokinetic analysis was conducted using noncompartmental methods with Model 200 of WinNonlin Enterprise (version 4.1; Pharsight, Mountain View, CA). The actual elapsed time after dosing was used to estimate all individual plasma PK parameters. When estimating the mean value for the concentration at a given time point, all not quantifiable (NQ) values were set to zero except when an individual NQ falls between two quantifiable values, in which case it was omitted from the calculation of mean profiles. Measurable concentrations which follow more than one consecutive mid-profile NQ were omitted (set to missing).

PBPK Model Structure

The overall structure of the lumped physiologically-based pharmacokinetic model investigated in this report is illustrated in Fig. 1a. Each intestinal segment is represented by a 4-compartmental model as depicted in Fig. 1b. In addition to compartments representing capillaries and lumen, the enterocytes are segregated into absorbing and non-absorbing compartments, toward the tip and base of the villi, respectively. The exact dividing line between the two compartments is a function of permeability as detailed later. The incorporation of absorbing and non-absorbing enterocyte compartments enables the model to characterize the two populations of enterocytes distinctively, including whether they participate in absorption (tip) or not (base), their volume, and distribution of CYP3A enzyme and therefore intrinsic clearance. Drug can move bi-directionally between the absorbing enterocyte compartment and the lumen and between enterocytes and the capillaries, as expected for passive permeation. It is recognized that the division of enterocytes into two compartments is only an approximation of the physiological reality, in the interest of mathematical simplicity, while in fact a more gradual transition is expected with drug exchange between neighboring enterocytes through the lateral regions of the basolateral membranes.

The physiological values and tissue/blood partition coefficients for midazolam are listed in Table I.

Gastrointestinal Compartments

Midazolam dose (D) is administered as a bolus into the stomach compartment, with A_{st} and V_{st} denoting the amount of drug in the stomach compartment. Drug transit from stomach to the first intestinal segment follows a first order process with k_{st} representing the first-order stomach emptying rate constant:

$$\frac{dA_{st}}{dt} = -k_{st}A_{st} + D\delta(t) \tag{1}$$

The differential equations governing the 4 compartments for each segment of intestine can be written as follows:

$$V_{il,i}\frac{dC_{il,i}}{dt} = \begin{cases} k_{st}A_{st} - k_{t,i}V_{il,i}C_{il,i} - PSA_{at,i}\left(C_{il,i} - f_{ue}C_{et,i}\right) + f_{ul}PSA_{cl}C_{lh}; & i = 1 \\ k_{t,i-1}V_{il,i-1}C_{il,i-1} - k_{t,i}V_{il,i}C_{il,i} - PSA_{at,i}\left(C_{il,i} - f_{ue}C_{et,i}\right); & i = 2,3 \end{cases} \tag{2}$$

$$V_{et,i}\frac{dC_{et,i}}{dt} = PSA_{at,i}\left(C_{il,i} - f_{ue}C_{et,i}\right) + PSA_{bt,i}\left(f_{ub}C_{ic,i} - f_{ue}C_{et,i}\right) - f_{ue}CL_{et,i}C_{et,i} \tag{3}$$

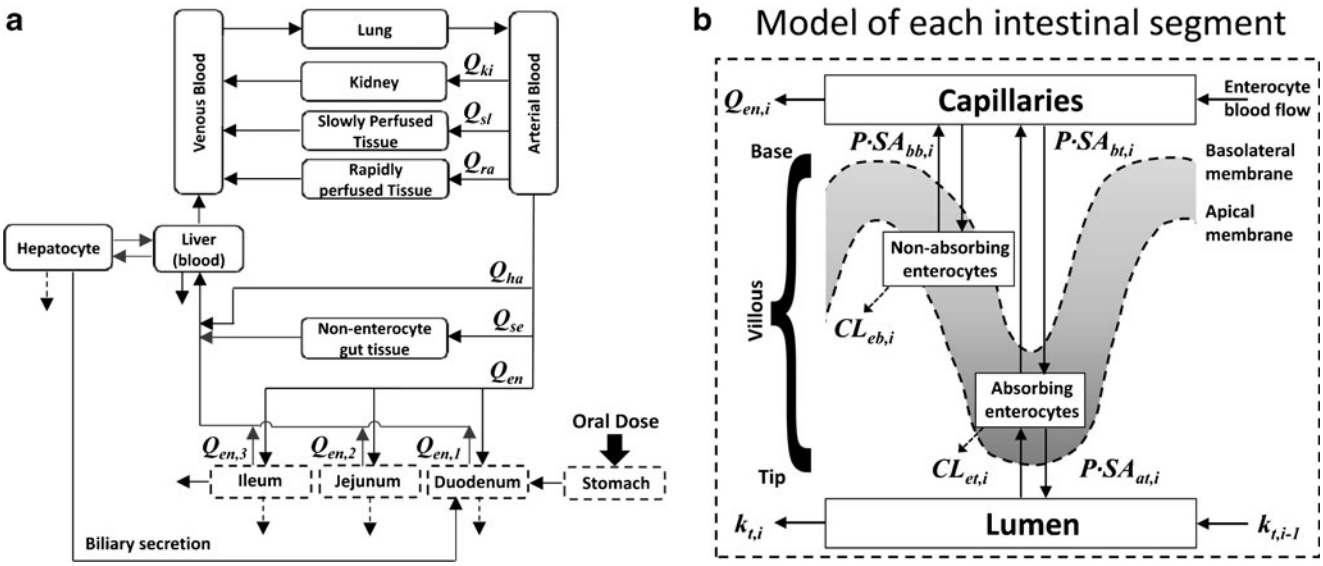

Fig. 1 (**a**) Diagram of the overall physiologically-based pharmacokinetic model of midazolam. With the exception of liver and enterocyte compartments, which are permeability-limited, all other tissue compartments including lung, kidney and slowly and rapidly perfused tissues are flow limited. A non-enterocyte gut tissue compartment is included as in the model developed by Cong *et al*. (8). Even though biliary excretion of midazolam is expected to be minimal, passive permeation of drug from hepatocytes,*via* bile, into the duodenal lumen is included to facilitate future expansion of the model. (**b**) 4-compartmental model for each intestinal segment. *Arrows with dashed lines* represent metabolism.

Table I PBPK Model Constants and Variables

Parameter	Value	Explanation
Blood flow (ml/hr)[1]		
Q_{co}	393078	Cardiac output
Q_{gw}	66823	17% of cardiac output
Q_{en}	18000	Enterocyte blood flow (7)
$Q_{en,1}$	1584	Duodenum (8.8% of enterocyte blood flow as in SimCYP®simulator)
$Q_{en,2}$	8712	Jejunum (48.4% of enterocyte blood flow as in SimCYP®simulator)
$Q_{en,3}$	7704	Ileum (42.8% of enterocyte blood flow as in SimCYP®simulator)
Q_{se}	48823	Remaining gut-wall
Q_{ha}	41273	Hepatic artery (including splenic and pancreatic blood flow)
Q_{ki}	66823	Kidney (17% of cardiac output)
Q_{sl}	119889	Slowly perfused tissues[3] (30.5% of cardiac output)
Q_{ra}	98270	Rapidly perfused tissues[4] (25% of cardiac output)
Tissue Volume (ml)[2]		
V_{total}	69000	Derived from a 69 kg body weight
V_{art}	1090	Arterial blood (1.84% of body weight, adjusted for vascular space in the liver and enterocytes)
V_{ven}	2957	Venous blood (4.99% of body weight, adjusted for vascular space in the liver and enterocytes)
V_{gw}	1263	Gut-wall (1.83% of body weight)
$V_{en,1}$	18.2	enterocytes in duodenum (4)
$V_{en,2}$	65.8	enterocyte in jejunum (4)
$V_{en,3}$	38.3	enterocyte in ileum (4)
V_{se}	1141	remaining gut-wall
$V_{il,i}$	Calc[6]	Volume of the intestinal lumen compartment (i = 1,2,3)
V_{ki}	317	Kidney (0.46% of body weight)
V_{li}	1608	Liver (2.33% of body weight)
V_{lu}	483	Lung (0.70% of body weight)
V_{sl}	53592	Slow tissues (77.67% of body weight)
V_{ra}	7024	Rapid tissues (10.18% of body weight)
f_{ve}	0.25	Vascular fraction of enterocyte, used to calculate the volume of the intestinal capillary compartment, $V_{ic,i}$
f_{vl}	0.29	Vascular fraction for liver, used to calculate the volume of the hepatic blood compartment, V_{lc}
Gastro-intestinal Transit time (hr^{-1})		
k_{st}	3.5	Gastric emptying (44)
$k_{t,1}$	4.3	Duodenum (43)
$k_{t,2}$	1.7	Jejunum (43)
$k_{t,3}$	2.1	Ileum (43)
Intestinal Dimensions (cm)		
r_d	1.65	Radius of duodenum (SimCYP®simulator)
r_j	1.34	Radius of jejunum (SimCYP®simulator)
r_i	1.20	Radius of ileum (SimCYP®simulator)

Table I (continued)

Parameter	Value	Explanation
l_d	25	Length of duodenum (16)
l_j	190	Length of jejunum (16)
l_i	285	Length of ileum (16)
CYP Enzyme Contents (nmol)		
$CYP3A_h$	5490	Total CYP3A in liver (4)
$CYP3A_d$	9.7	Total CYP3A in duodenum (4)
$CYP3A_j$	38.4	Total CYP3A in jejunum (4)
$CYP3A_i$	22.4	Total CYP3A in ileum (4)
Surface Areas		
SA_{at}	Calc[6]	Apical surface area of the absorbing enterocyte compartment
SA_{bt}	Calc[6]	Basolateral surface area of the absorbing enterocyte compartment
SA_{bb}	Calc[6]	Basolateral surface area of the non-absorbing enterocyte compartment
Tissue/blood Partition Coefficient[5]		
k_{sl}	2.75	Slow tissue
k_{ra}	2.12	Rapid tissue
k_{en}	2.65	Enterocyte
k_{se}	2.65	Remaining gut tissue
k_{lu}	1.92	Lung
k_{ki}	1.45	Kidney
k_{li}	1,48	Liver
Other Variables		
P	Fitted[7]	Permeability across a single membrane
P_{app}	Calc[6]	Permeability across both apical and basolateral membrane
CLu_{int}	Fitted[7]	Unbound intrinsic clearance per pmol enzyme
CL_h	Calc[6]	Unbound intrinsic clearance of the liver
$CL_{et,i}$	Calc[6]	Unbound intrinsic clearance of the absorbing enterocyte compartment
$CL_{eb,i}$	Calc[6]	Unbound intrinsic clearance of the non-absorbing enterocyte compartment
$V_{et,i}$	Calc[6]	Volume of the absorbing enterocyte compartment
$V_{eb,i}$	Calc[6]	Volume of the non-absorbing enterocyte compartment
F_{as}	Fitted[7]	Apical amplification factor
F_{bs}	Fitted[7]	Basal amplification factor

[1] *adapted from ICRP publication 89 (International Commission on Radiological Protection, 2002) converted to 69 kg body weight using simple normalization,*

[2] *adapted from ICRP publication 89, converted for 69 kg subjects using power rule with exponent of 0.75 according to Brown et al. (46)*

[3] *Slowly perfused = adipose, bone, muscle and skin*

[4] *Rapidly perfused = all others*

[5] *Individual tissue partition coefficients are from Fenneteau et al. (45). The partition coefficients for slowly (adipose, bone, muscle and skin) and rapidly (using brain and heart as representative tissues) perfused tissues were calculated as weighted averages of individual tissue partition coefficients.*

[6] *Calculated using equations described in the text*

[7] *Optimized parameter*

$$V_{eb,i}\frac{dC_{eb,i}}{dt} = PSA_{bb,i}\left(f_{ub}C_{ic,i} - f_{ue}C_{eb,i}\right) - f_{ue}CL_{eb,i}C_{eb,i} \quad (4)$$

$$V_{ic,i}\frac{dC_{ic,i}}{dt} = Q_{en,i}\left(C_b - C_{ic,i}\right) - PSA_{bt,i}\left(f_{ub}C_{ic,i} - f_{ue}C_{et,i}\right) - PSA_{bb,i}\left(f_{ub}C_{ic,i} - f_{ue}C_{eb,i}\right) \quad (5)$$

C_{il}, C_{et}, C_{eb} and C_{ic} denote the drug concentration in the intestinal lumen, absorbing enterocyte at the villous tips, non-absorbing enterocytes at the villous base and intestinal capillaries, respectively, with V_{il}, V_{et}, V_{eb} and V_{ic} denoting the volumes of the corresponding compartments. The free fraction in the enterocyte, f_{ue}, is calculated as the free fraction in blood (f_{ub}) divided by the enterocyte tissue/blood partition coefficient (k_{en}).

The subscript i ($i=1, 2$ or 3) denotes the segment of intestine. Drug transit from one intestinal segment to the next is modeled as a first-order process with a rate constant $k_{t,i}$. Drug movement between intestinal lumen and absorbing enterocytes and between absorbing enterocytes and capillaries is determined by drug permeability, P, assumed to be the same across apical and basolateral membranes of the enterocyte. The last term $f_{ul}PSA_{cl}C_{lh}$ in Eq. 2 represents the passive permeation of midazolam from the hepatocyte across the canalicular membrane into the duodenal lumen (biliary excretion), and is described in further detail in the "Liver Compartments" section.

Apical Surface Area and Volume of the Enterocyte Compartments

The area of the human intestine available for drug absorption can be up to 30 times greater than the cylindrical surface area, with the plicae circulars increasing the surface area by a factor of 3 and the finger-like villi, extending from the intestinal wall, by an additional factor of 10 (16).

In the present work it is assumed that only a portion of the enterocytes, starting from the tip of the villous, engage in drug exchange with the lumen. This is represented by the parameter F_{as}, the apical surface amplification factor, which, when multiplied by the cylindrical surface area ($2\pi r_i l_i$) yields the total apical surface area of the absorbing enterocytes, $SA_{at,i}$. F_{as} is assumed to be identical in the three intestinal segments and has a value less than 30 (with a value of 30 absorption occurs along the entire villous surface). While F_{as} is also implicitly assumed to depend on permeability, this dependency was not explicitly modeled in the present work. Instead, it was treated as an independent model parameter fitted to the midazolam data. The value of F_{as} that best fit the data was compared to the value theoretically estimated by Oliver *et al.* (13)), based on villous dimensions, aqueous diffusion coefficient and water absorption rate, as an independent verification of the present model. For simulations using the current model to investigate the effect of permeability on various model outputs, F_{as} associated with each permeability value was estimated using Eq. 17 from Oliver *et al.* (13).

$SA_{ab,i}$, the apical surface area of the non-absorbing enterocytes is calculated as the difference between the theoretical maximal surface area (30 times cylindrical surface area) and surface area of the absorbing enterocytes, $SA_{at,i}$.

The volumes of the absorbing and non-absorbing enterocyte compartments for each of the intestinal segments, $V_{et,i}$ and $V_{eb,i}$ can then be defined below as a fraction of the total enterocyte volume ($F_{as}/30$ or $1-F_{as}/30$) in each intestinal segment, $V_{e,i}$.

Basolateral Surface Area of the Enterocyte Compartments

A scaling factor, F_{bs}, is used in the present model to account for any potential difference between the apical surface area of the enterocytes and basolateral enterocyte surface area or the corresponding capillary surface areas, $SA_{bt,i}$ and $SA_{bb,i}$.

The presence of microvilli on the apical but not on the basolateral membrane of the enterocytes could contribute to a difference between the apical and basolateral surface areas. The presence of microvilli amplifies the apical surface by a factor of 20 (16). However, the enterocytes are columnar cells with height and width of approximately 30 um and 6 um respectively (48) and bounded to the adjacent enterocytes by tight junctions at the luminal side. Using these dimensions and assuming hexagonal geometry, the basolateral surface can be calculated to be 21 times larger than apical surface, approximately offsetting the amplication of the apical surface due to microvilli.

Available literature data on the surface area of the capillary bed is scarce and variable. Krogh (17) noted that the surface area of villous capillaries in dog jejunum and rabbit intestine is equal to 80–90% of the villous surface area. Casley-Smith *et al.* (18) estimated that in cat jejunum the capillary surface area is 5 cm^2/g at the base and 29 cm^2/g in the upper region of the villous. Since the villous surface area in the cat is about 30 cm^2/g tissue (12,19), it can be deduced that the surface area of villous capillaries in cats is between 17 and 100% of the total villous surface area.

Exploratory modeling analysis revealed that optimization of this parameters resulted in a large coefficient of variation, indicating possible multiple solutions. Based on the above considerations F_{bs} was therefore fixed at 1 in the final analysis.

Permeability

Passive permeability (normalized by surface area) through the apical and basolateral plasma membranes of enterocytes and hepatocytes are all assumed to be identical, whereas the permeability clearances are calculated as the product of permeability and surface area.

The permeability is defined in this model as diffusion across each of the apical and basolateral membranes individually. In order to facilitate comparison to the permeability estimated from *in vitro* MDCK or Caco-2 cell experiments it is re-parameterized as $P=2\ P_{app}$, where P_{app} is the permeability across both apical and basolateral membranes, equivalent to what is measured in the *in vitro* MDCK or Caco-2 cell experiments.

Intrinsic Clearance

The unbound intrinsic clearance per unit of CYP3A enzyme (CLu_{int}) is assumed to be identical between the liver and small intestine, as supported by previously reported turn over values which were not significantly different for intestinal and liver samples (5,47). The intrinsic clearance of the whole liver (CL_h) is therefore computed by multiplying CLu_{int} by the total abundance of the enzyme in the liver.

Due to the paucity of quantitative information on the distribution of CYP3A enzyme along the villous-crypt axis, three distribution patterns were considered in the present work. In each case, the intrinsic clearance for the absorbing and non-absorbing enterocytes, $CL_{et,i}$ and $CL_{eb,i}$, are calculated by multiplying the intrinsic clearance per unit enzyme, CLu_{int}, with the amount of enzyme assigned to each compartment.

Distribution Pattern 3: Uniformly distributed CYP3A enzyme. Since CYP3A enzyme in each segment of intestine is assumed to be uniformly distributed in the enterocytes along the villous-crypt axis, the amount of enzyme in absorbing and non-absorbing compartments is directly proportional to the fraction of total enterocyte volume attributed to each compartment.

$$CL_{et,i} = CLu_{\text{int}}\left(\frac{F_{as}}{30}\right) CYP_{en,i} \tag{6}$$

$$CL_{eb,i} = CLu_{\text{int}}\left(1-\frac{F_{as}}{30}\right) CYP_{en,i} \tag{7}$$

$\text{CYP}_{\text{en,i}}$ denotes the total amount of CYP enzymes in each intestinal segment.

Distribution Pattern 3: CYP3A enzyme density increases linearly along the crypt–villous axis. In this scenario, it is assumed that CYP3A enzyme is absent in the cells at the very base of the villous but the enzyme density increases linearly along the crypt-villus axis, reaching peak levels at the villous tip. The amount of CYP3A in the non-absorbing enterocyte compartment at the base is computed by integrating the linear density function along the crypt-villous axis, resulting in a quadratic function of the fractional volume of the base enterocyte compartment in Eq. 9 below. The remaining enzyme is in the absorbing compartment at the tip (Eq. 8).

$$CL_{et,i} = CLu_{\text{int}}\left\{1-\left(1-\frac{F_{as}}{30}\right)^2\right\} CYP_{en,i} \tag{8}$$

$$CL_{eb,i} = CLu_{\text{int}}\left(1-\frac{F_{as}}{30}\right)^2 CYP_{en,i} \tag{9}$$

Distribution Pattern 3: CYP3A enzyme is contained entirely in the absorbing enterocyte compartment. Since CYP3A enzyme is entirely contained in the absorbing enterocyte compartment, the intrinsic clearance for the non-absorbing enterocyte compartment is zero.

$$CL_{et,i} = CLu_{\text{int}}\ CYP_{en,i} \tag{10}$$

$$CL_{eb,i} = 0 \tag{11}$$

Liver Compartments

The differential equations governing the 2 compartments representing liver can be written as follows:

$$V_{lc}\frac{dC_{lc}}{dt} = Q_{ha}C_b + Q_{se}\frac{C_{se}}{k_{se}} + \sum_{i=1}^{3} Q_{en,i}C_{ic,i} - \left(Q_{ha} + Q_{se} + \sum_{i=1}^{3} Q_{en,i}\right)\cdot C_{lc} - PSA_{bl}\left(f_{ub}C_{lc} - f_{uh}C_{lh}\right) \tag{12}$$

$$V_{lh}\frac{dC_{lh}}{dt} = PSA_{bl}\left(f_{ub}C_{lc} - f_{uh}C_{lh}\right) - f_{uh}\left(CL_h + PSA_{cl}\right)\cdot C_{lh} \tag{13}$$

C_{lh} and C_{lc} denote the drug concentration in the hepatocytes and hepatic blood, respectively, with V_{lh} and V_{lc} denoting the volumes of the corresponding compartments. C_{se} and k_{se} are the drug concentration and partition coefficient of the compartment representing the innate components of the gut, respectively, *i.e.* the non-enterocyte component. The free fraction in the hepatocyte, f_{uh}, is calculated as the free fraction in blood (f_{ub}) divided by the liver/blood partition coefficient.

Drug transport across the hepatocyte basolateral membrane is modeled as passive diffusion, with permeability denoted as P (assumed to be the same as that for enterocyte membranes). SA_{bl} and SA_{cl} denote the area of the basolateral (sinusoidal) and canalicular surfaces of the hepatocyte. Transport across the canalicular membrane results in biliary

excretion into the duodenal lumen, as mentioned previously. Metabolism of midazolam in the hepatocyte is modeled as a first-order process, with intrinsic clearance CL_h.

Hepatocyte Sinusoidal and Canalicular Surface Areas

Based on stereological analysis Blouin *et al.* (20) estimated the hepatocyte plasma membrane surface area to be 5,630 cm^2/g liver tissue. They also found that 72% of the plasma membrane surface area is sinusoidal. Keppler and Arias (21) have shown that 10–15% of the plasma membrane surface area is canalicular. A value of 12.5% is used in the present model. Consequently, the hepatocyte sinusoidal and canalicular surface areas, SA_{bl}, and SA_{cl}, are calculated to be 4053.6 and 675.6 cm^2/g of liver tissue, respectively.

Intestinal and Hepatic Availability

Intestinal and hepatic availability (F_g and F_h) are calculated as the ratio of the model-predicted net flux of drug escaping metabolism over the net flux of incoming drug for each tissue, respectively.

Model Development Approach

The model developed in the present study was used to fit both the midazolam blood concentration time profile and the fraction of absorbed drug escaping intestinal first-pass extraction, F_g, simultaneously. Only 3 parameters were optimized (CLu_{int} P_{app} *and* F_{as}) while others were held constant.

Parameter optimization was performed using the SAAM II program (version 2.0, SAAM Institute, Seattle, WA). Model discrimination was based on the values of the Akaike information criterion (AIC) and visual inspection of the goodness of fit plots. Simulations were carried out in SAAM II using the Rosenbrock integration method.

Absorption Surface Area Calculation

Equation 17 (Model II: Intervillous Diffusion with Convection Induced by Water Flux) from Oliver *et al.* (13) was used to calculate surface accessibility ($=F_{as}/30$) at each permeability for model simulations performed to explore the relationship between permeability and F_g and F_h as well as how permeability influences the extent to which a change in CLu_{int} is affecting F_g and F_h. For simplicity, dimensions of villi (width: 100 μm, height: 600 μm) and inter-villous width (40 μm) for human jejunum found in Strocchi and Levitt (22) were used for all intestinal segments. Aqueous diffusion coefficient of 6.63×10^{-6} cm^2/s and a moderate net water absorption flow rate of 5×10^{-4} cm/s were used for the calculations.

RESULTS

Midazolam Plasma Levels Following Oral Administration

Plasma concentration-time profiles (mean ± SD) of midazolam after a single oral dose of 5 mg are shown in Fig. 2. The corresponding pharmacokinetic parameters are listed in Table II. Plasma concentrations rise rapidly following dosing, reaching peak concentrations within 0.25–2 hr post dosing, and decline with a terminal t½ ranging from 2–8 hr. The mean Cmax of 21.3 ng/mL and AUC (0→t) of 68.2 ng*hr/mL as well as the estimated oral plasma clearance (CL/F) of 16.2 mL/min/kg in the current studies is consistent with other studies (15,23–26).

Model Fitting Results

All three versions of the model, differing only in the assumed distribution of CYP3A along the crypt-villous axis, adequately predicted the biphasic nature of the midazolam blood concentration profile and the intestinal availability (F_g) simultaneously. The values of the best fitting model parameters are summarized in Table III. Statistically, the version assuming CYP3A enzyme density increases linearly along the crypt–villous axis (distribution pattern 2) yields the best fit to the data (AIK = −2.08, BIC = −1.99). The midazolam blood concentration-time profile and the F_g calculated by the best fit model are plotted in Fig. 3. Even though the other two versions of the model (CYP3A distribution patterns 1 and 3) yield statistically worse fits to the data, the model predicted blood concentration-time profile and intestinal availability F_g are visually indistinguishable from those predicted by the best fitting model.

A simulated intravenous midazolam concentration time profile was generated using the best fitting model parameters (CYP3A distribution pattern 2) to calculate pharmacokinetic parameters using non-compartmental methods. The computer

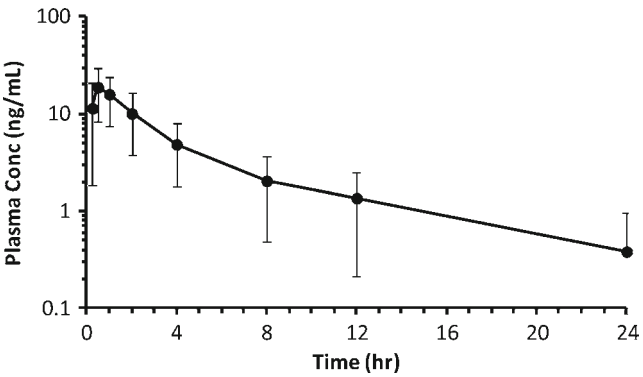

Fig. 2 Observed midazolam plasma concentration time course following a single 5 mg oral administration to healthy postmenopausal female subjects. Symbols represent mean (± SD) ($n = 82$).

Table II Summary of Selected Midazolam Pharmacokinetic Parameters

Plasma Midazolam PK Parameter	Midazolam Dose (5 mg)	
	Geometric Mean (95% CI)	Arithmetic Mean (%CV)
AUC(0-∞) (ng.h/mL)	62.8 (52.3–73.4)	74.6(65.2)
AUC(0-t) (ng.h/mL)	57.2 (47.6–66.7)	68.2 (64.5)
Cmax (ng/mL)	19.2 (17–21.4)	21.3 (47.2)
t1/2 (h)	4.5 (3.9–5.1)	5.1 (51.6)
tmax (h)	0.5[1] (0.2–2.0)	0.7 (58.3)

Source Data:

[1] tmax was presented as median (range)

simulated plasma clearance, volume of distribution at steady-state, terminal half-life and oral bioavailability are within the range reported in the literature (Table IV) (15,25–27).

All subsequent model simulations, unless specifically mentioned otherwise, are performed using the best fitting model.

Distinction Between Absorbing and Non-Absorbing Enterocyte Compartments

Previous modeling efforts treat the effective permeability and volume of the enterocyte compartment as two unconnected parameters. Effective *in vivo* permeability is typically estimated from *in vitro* permeability experiments using empirical equations to account for the surface area involved in *in vivo* absorption (7). The enterocyte compartment on the other hand, is modeled as one homogeneous compartment involving all enterocytes, implicitly assuming that drug absorption and metabolism occurs equally over the entire villous surface. In contrast, the present work recognizes explicitly that the effective *in vivo* permeability and the proportion of enterocytes participating in absorption and metabolism are inextricably linked through the surface area accessible for absorption. A greater absorption surface area translates simultaneously into a higher effective permeability as well as an increased proportion of absorbing enterocytes and *vice versa*. This necessitates a distinction between absorbing and non-absorbing enterocyte compartments, in which the volume and CYP3A content (intrinsic clearance) of each compartment varies with the surface area accessible for absorption.

Computer simulation can be used to dissect the effect of volume and intrinsic clearance adjustments so that they can be examined individually (Fig. 4). Since the volume of the absorbing enterocyte compartment is smaller than the sum of the absorbing and non-absorbing compartments, the rate at which drug concentration changes in this compartment will be faster than if the enterocyte compartment is modeled as a single homogeneous compartment. Correcting for the absorbing enterocyte compartment volume alone will therefore result in a more rapid change in enterocyte free drug concentrations as a function of time, with a higher maximal free drug concentration (Fig. 4a, long dashed line *versus* short dashed line). It should be noted that the net effect of this volume correction alone without a concomitant adjustment of CYP3A4 content does not result in a change in enterocyte exposure. The AUC for both scenarios is the same. This can also be demonstrated mathematically by

Table III PBPK Model Parameters

Parameter	Explanation	Unit	Best fit parameter values (%CV)		
			CYP only in the tip enterocytes	Uniformly Distributed CYP	CYP increase linearly toward the tip
CLu_{int}[1]	Intrinsic clearance per unit CYP3A enzyme[1]	μL/min/pmol	1.5 (23.9%)	3.5 (8.3%)	2.8 (7.9%)
CL_h[2]	Hepatic intrinsic clearance[2]	L/hr	477.4	1134.8	912.7
P_{app}	Permeability	$\times 10^{-6}$ cm/s	107.3 (19.4%)	38.8 (10.5%)	50.7 (10.4%)
F_{as}	Apical amplification factor	No unit	4.1 (44.0%)	14.0 (32.7%)	9.6 (33.7%)
Total objective function			−5.82	−6.67	−6.90
AIC			−1.54	−1.96	−2.08
BIC			−1.45	−1.87	−1.99

[1] Intrinsic clearance is assumed to be same between hepatic and intestine after normalizing by weight and CYP content

[2] Computed from CLu_{int} (ul/min/pmol) by multiplying with the CYP contents in the liver

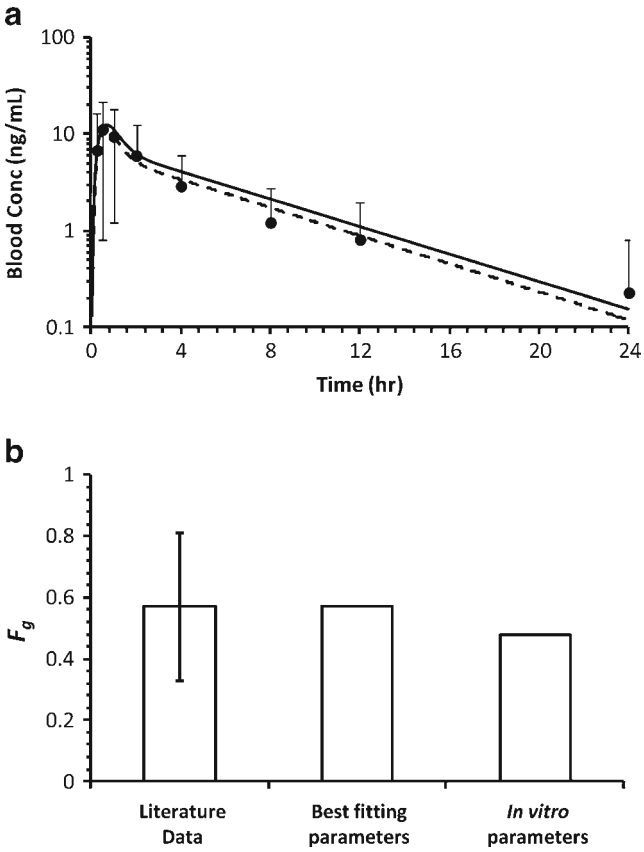

Fig. 3 Observed and model predicted time course of midazolam blood concentration (**a**) and intestinal availability (**b**) following a single 5 mg oral administration to healthy postmenopausal female subjects. Symbols represent mean (± SD) blood concentrations ($n = 82$). Solid line represents the model-fitted profile (with CYP3A enzyme distribution 2), while the dashed line represents the model predicted profile using representative literature values for *in vitro* CLu_{int} and P_{app} (3.4 μl/min/pmol and 40×10^{-6} cm/s, respectively). The standard deviation for F_g was from Thummel *et al.* (15) and assuming identical standard deviation for F_g and E_g.

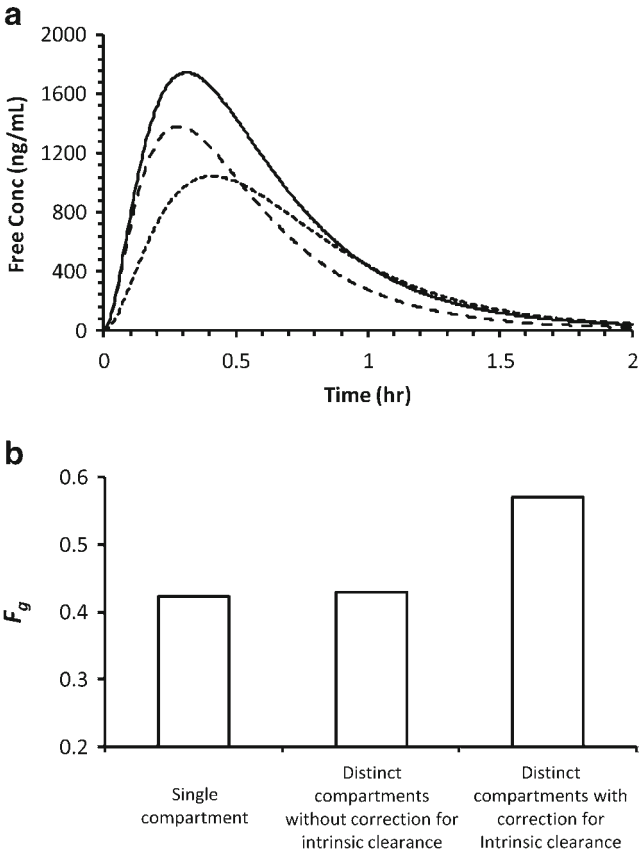

Fig. 4 Computer simulation demonstrating the impact of making a distinction between absorbing and non-absorbing enterocyte compartments on enterocyte free concentration in duodenum (**a**) and intestinal availability (**b**). Simulation performed using the best fitting model assuming CYP3A enzyme density increases linearly along the crypt–villous axis. Three scenarios were simulated, including a single enterocyte compartment (*short-dashed line*), distinct absorbing and non-absorbing enterocyte compartments without correction for intrinsic clearance (long dashed line), and with correction for intrinsic clearance according to Eqs. 8 and 9 (*solid line*).

Table IV PK Parameters Calculated Based on Best Fitting Model

Parameter	Model Calculated Values	Literature Values[1] (reference)
CL (L/hr)	19	22.2 (15) 32.8 (25) 24.8 (26) 25.9 (27)
Vss (L)	94.6	60.9 (15) 147 (25) 84 (26)
Terminal T½(hr)	4.2	2.5 (15) 4.1 (25) 2.8 (26)
% F	36.7	30% (15) 41% (25) 31% (26) 25.5% (27, inferred[2])

[1] Unit conversion as needed based on 70 kg body weight

[2] Inferred from the ratio of the reported intravenous and oral plasma clearances

solving the differential equations governing these rate processes.

Because not all intestinal CYP3A will be in the absorbing enterocyte compartment, the intrinsic clearance will be lower than if the enterocyte is modeled as a single homogeneous compartment. This further adjustment for CYP3A content in addition to the volume correction will result in both a more rapid change in enterocyte free drug concentration, a further increase in maximal free drug concentration (as well as an increase in AUC, compared to the single enterocyte compartment (Fig. 4a, solid line *versus* short dashed line). This will also result in a lower extent of metabolism and therefore higher intestinal availability (Fig. 4b). The aforementioned effect should be most notable for highly permeable drugs where absorption occurs only in the upper regions of the villous. As the villous surface accessible for absorption increases with reduced permeability, the volume of the absorbing enterocyte compartment also increases. At a permeability of 2×10^{-6} cm/s

or lower the villous surface accessible for absorption exceeds 90% (estimated using Eq. 17 from Oliver *et al.* (13). At this low permeability range, the volume of the absorbing enterocyte compartment approaches that of the total enterocyte compartment volume and the non-absorbing compartment is essentially non-existing, a situation indistinguishable from a single homogeneous enterocyte compartment.

Free Fraction in Enterocytes

It is worth noting that the model can achieve a good prediction of midazolam intestinal availability and blood concentration-time profile without assuming the absence of drug binding in enterocytes, as in Yang *et al.* (7) or Gertz *et al.* (9), an assumption that cannot readily be physiologically justified. While the free drug concentration in a tissue can vary depending on the rates of equilibration of drug moving in and out of the tissue, binding to tissue proteins and lipids is typically assumed to occur very rapidly, such that a constant free fraction in the tissue is maintained.

It can be shown mathematically that the intestinal availability, F_g, in the present model is dependent on the relative magnitudes of intestinal CYP3A metabolism and permeation of drug across the enterocyte basolateral membranes. Since both processes are modeled to be directly proportional to the free drug concentration in the enterocyte, a change in free drug concentration in the enterocyte will change both processes by the same proportion. While this will change the rate of drug entering the portal vein, it will have no effect on the intestinal extraction ratio. This point is illustrated in Fig. 5, in which progressively lower free enterocyte fraction (f_{ue}) resulted in lower model predicted C_{max} values due to lower permeation rates but which have no effect on intestinal extraction or AUC.

Free Drug Concentration in Enterocytes and Hepatocytes

As shown in Fig. 6a, the present model predicts that, even though the enterocyte and hepatocyte tissue partition coefficients of midazolam used in the model differ only by approximately 2-fold, the free drug concentration in the absorbing enterocyte compartment can be as much as 1,000-fold higher than that in the hepatocyte compartment. This is the result of a combination of factors including the separation of the blood flow to the enterocyte layer from the rest of the gut tissue (*e.g.* serosa), division of the intestines into several segments, the introduction of permeability limitation and separate absorbing and non-absorbing enterocyte compartments into the model. Since midazolam is theorized to be absorbed only through enterocytes at the villous tip, the free drug concentration in the enterocytes at the base of the villous, receiving drug from systemic blood flow only, is expected to be lower, as demonstrated in Fig. 6b.

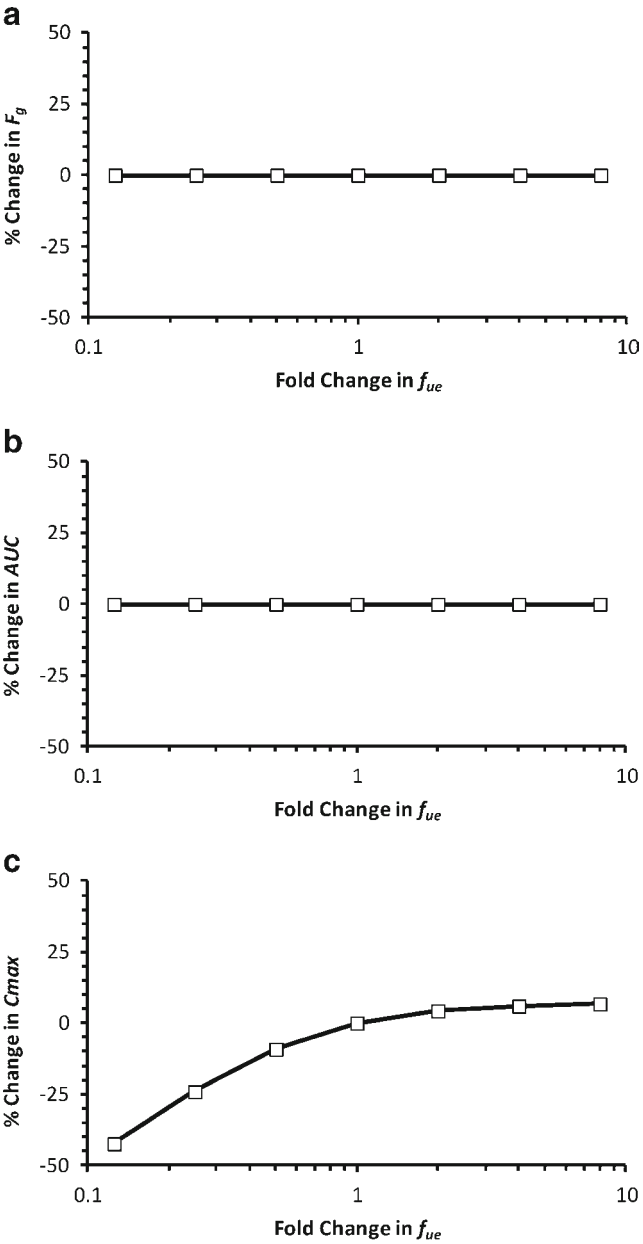

Fig. 5 Computer simulation demonstrating the effect of free fraction in the enterocyte, f_{ue}, on F_g, *AUC* and *Cmax*. Simulation performed using the best fitting model assuming CYP3A enzyme density increases linearly along the crypt–villous axis.

Figure 6c demonstrates how the concentration in the absorbing enterocyte compartment depends on the distribution of CYP along the crypt-villous axis. The concentration in the enterocyte is determined by the balance between permeability across the basolateral membrane and intrinsic clearance, *i.e.* CYP3A content. When permeability is kept constant at that of midazolam, higher intrinsic clearance will result in lower enterocyte concentration. If CYP3A is assumed to be entirely contained in the absorbing enterocyte compartment (distribution pattern 3),

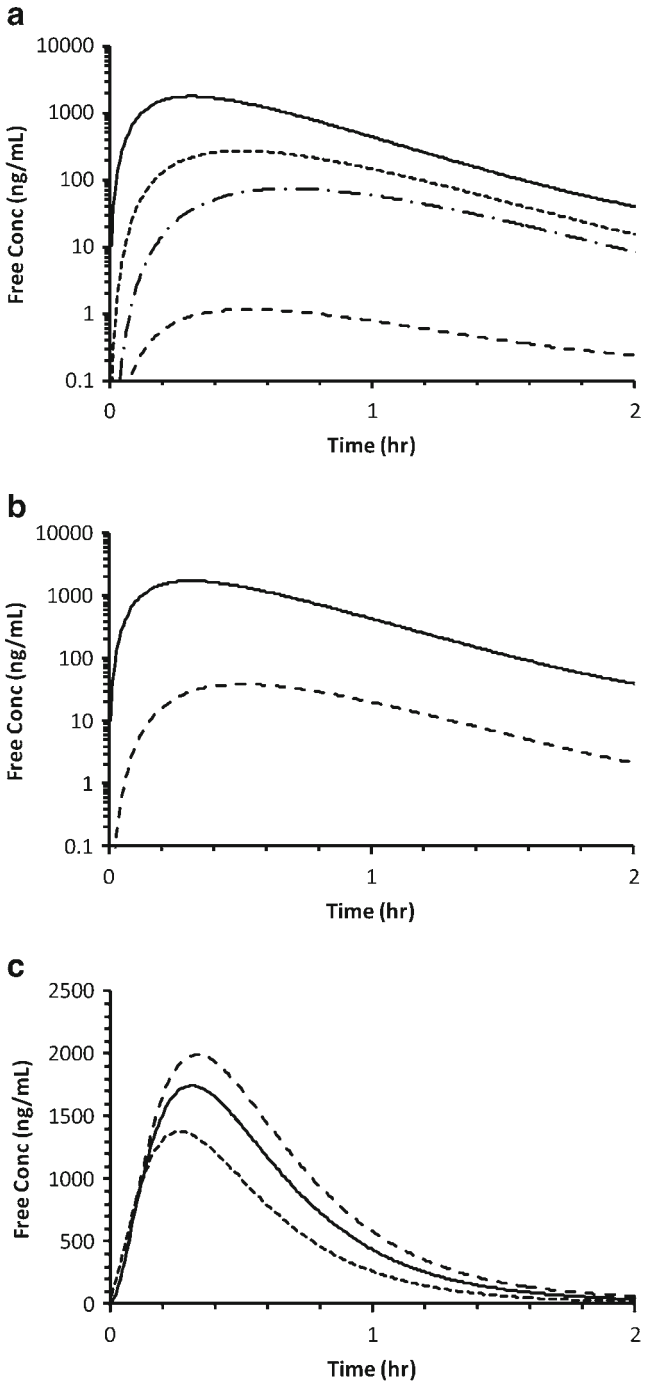

Fig. 6 (**a**) Computer simulated time courses of unbound drug concentration in liver (*long dashed line*) and the absorbing enterocyte compartments of duodenum (*solid line*), jejunum (*short dashed line*) and ileum (*dash-dot line*). (**b**) Computer simulated unbound drug concentration in the duodenum absorbing (*solid line*) and non-absorbing (*dashed line*) enterocyte compartments. Simulations for (**a**, **b**) were performed using the best fitting model assuming CYP3A enzyme density increases linearly along the crypt–villous axis. (**c**) Computer simulated unbound drug concentration in the duodenum absorbing enterocyte compartment for the 3 different distributions of CYP3A along the crypt-villous axis; CYP3A increases linearly along the villous axis (distribution pattern 2; *solid line*), uniformly distributed CYP3A (distribution pattern 1; *long dashed line*) and CYP3A only present in the absorbing enterocyte compartment (distribution pattern 3; *short dash line*). CLu_{int} was assumed to be 2.8 μL/min/pmol for all 3 cases.

the intrinsic clearance in the absorbing enterocyte will be higher than if CYP3A is distributed evenly along the crypt-villous axis (distribution pattern 1), and will therefore result in a lower free concentration in the absorbing enterocyte compartment. If the density of CYP3A enzyme is assumed to increase linearly along the crypt-villous axis (distribution pattern 2) the distribution of CYP3A enzymes shifts toward the villous tip but not as severely as in distribution pattern 1, and therefore results in intermediate enterocyte concentrations.

Effect of Permeability on Intestinal and Hepatic First Pass Extraction and Systemic AUC

Permeability has the opposite effect on hepatic and intestinal first-pass extraction. In the liver, the drug molecule is delivered to the hepatocyte by its blood supply. Lower permeability limits drug molecules from reaching the site of metabolism within hepatocytes, reducing hepatic metabolism and thereby increasing the fraction of drug escaping hepatic first-pass, F_h (Fig. 7a). The situation is reversed in the intestine. The majority of the drug is delivered to the enterocytes from the lumen. Decreasing the rate at which molecules diffuse across basolateral enterocyte membranes (decreasing permeability, P_{app}) results in an increased enterocyte residence time, thus lower intestinal availability (F_g). Figure 7b also demonstrated that, although the differences in the calculated F_g among the three CYP3A distribution patterns considered are not great, F_g is predicted to be lowest if CYP3A is assumed to be entirely contained in the absorbing enterocyte compartment (distribution pattern 3, short dashed line) and highest if CYP3A is assumed to be uniformly distributed (distribution pattern 1, long dashed line). The differences however diminished at low permeability. It should be noted that the curves in Figs. 7 and 8 can shift either to the right or left if different surface areas are used in the calculations.

The model calculated relationship between permeability and AUC in Fig. 7d, using the CLu_{int} of midazolam from the best fitting model, is the net result of a complex interaction between multiple counteracting factors. For a 10-fold increase in relatively low permeability from 1×10^{-6} to 10×10^{-6} cm/s, the intestinal surface accessibility is reduced by 28% (Fig. 7c; calculated based on the theoretical derivation by Oliver *et al.* (13) while the fraction of drug escaping intestinal first-pass (F_g) increased by approximately 4-fold. However, over the same 10-fold increase in permeability, drug escaping hepatic first-pass (F_h) decreased by approximately 30%. This resulted in a net increase in AUC. These countering effects on AUC, however, balanced out in the higher permeability range, resulting in minimal change in AUC for a permeability increase from 10×10^{-6} to 100×10^{-6} cm/s.

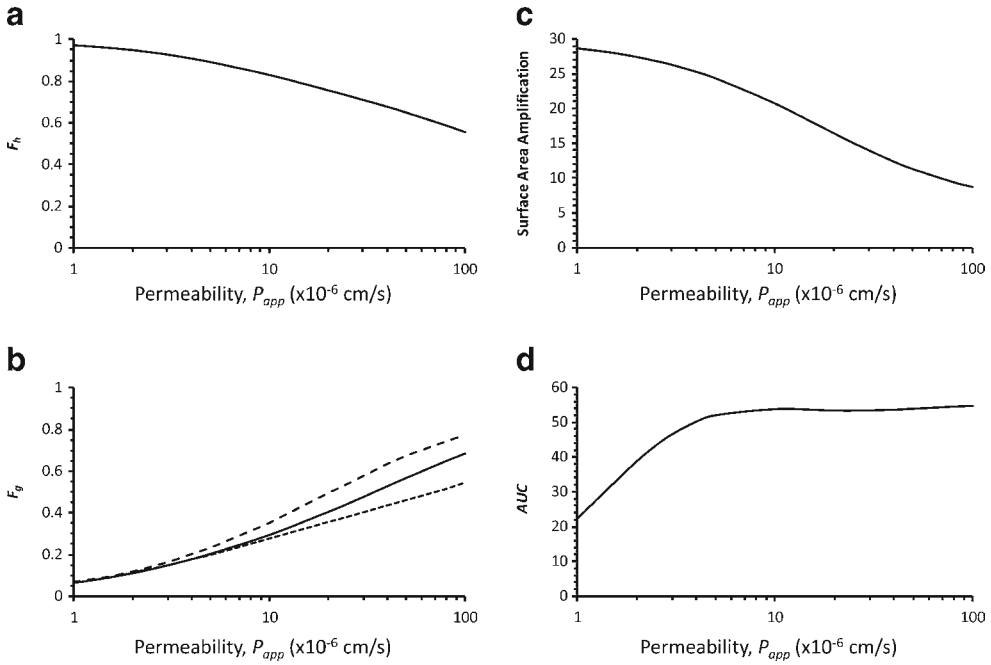

Fig. 7 Computer simulations comparing the effect of permeability on F_h (**a**), F_g (**b**), intestinal surface area amplification factor (**c**) and blood AUC (**d**) assuming CYP3A increases linearly along the villous axis (distribution pattern 2; *solid line*). CLu_{int} that best fit the midazolam data was used in the simulation. Permeability-dependent intestinal surface area accessibility was calculated for human jejunum using the equations derived by Oliver *et al*. (13). Effect of permeability on F_g was also simulated for uniformly distributed CYP3A (*long dashed line*) and CYP3A present only in the absorption enterocyte compartment (*short dashed line*). A CLu_{int} of 2.8 μL/min/pmol was used for all 3 CYP3A distributions. The curves can shift either to the right or left depending on the surface areas are used in the calculations.

Effect of Victim and Perpetrator Drug Permeability on the Magnitude of CYP3A mediated DDIs in intestine and liver

The effect of changes in intrinsic clearance on F_g and F_h (*via* CYP3A inhibition or induction) are also dependent on permeability of the drug (Fig. 8). In this respect, one must again keep in mind the opposite effect of permeability in limiting extraction in intestine *versus* liver.

As demonstrated in Fig. 8a, at the low end of the permeability range, transit of drug from blood into hepatocytes becomes the rate-limiting step of hepatic metabolism. Therefore even large changes in intrinsic clearance (CYP3A inhibition or induction) have limited impact on hepatic extraction ratio. As permeability increases and the drug molecule can move into the hepatocyte more readily, permeability becomes less rate-limiting, and hepatic extraction becomes much more sensitive to changes in intrinsic clearance.

The situation with intestinal metabolism is more complicated, as the permeability of both victim and perpetrator drugs must be taken into consideration. Perpetrators with sufficiently low permeability will be absorbed through most of the villous surface and thereby affect most enterocytes (*e.g.* 90% of villous surface accessible for absorption at a permeability of 2×10^{-6} cm/s as mentioned previously). The dash-lines in Fig. 8b approximate such a situation by simulating a 4-fold increase (induction) or decrease (inhibition) in the intrinsic clearance of all enterocytes. F_g is less sensitive to changes in intrinsic clearance when the permeability of the victim drug is high enough because the rate at which drug escapes the enterocytes is much greater than the rate of intestinal metabolism. As the permeability of the victim decreases, the rate of metabolism increases relative to that of escape from the enterocyte and F_g becomes more sensitive to changes in intrinsic clearance.

However, it can be deduced from the model that a highly permeable perpetrator drug can only exert its full effect on a highly permeable victim drug. Its effectiveness is progressively weakened as the permeability of victim decreases below that of the perpetrator. This is because, according to the present model, the highly permeable perpetrator drug is only absorbed through and inhibits the CYP3A enzymes in enterocytes at the villous tips, whereas a portion of a less permeable victim drug is absorbed through enterocytes toward the villous base unaffected by the perpetrator.

DISCUSSION

A key feature of the current model is that the surface area for absorption is directly linked to the volume and CYP3A content of the underlying enterocyte compartment. As such, it provides a more realistic estimate of free and total enterocyte drug concentration and intestinal first pass metabolism than

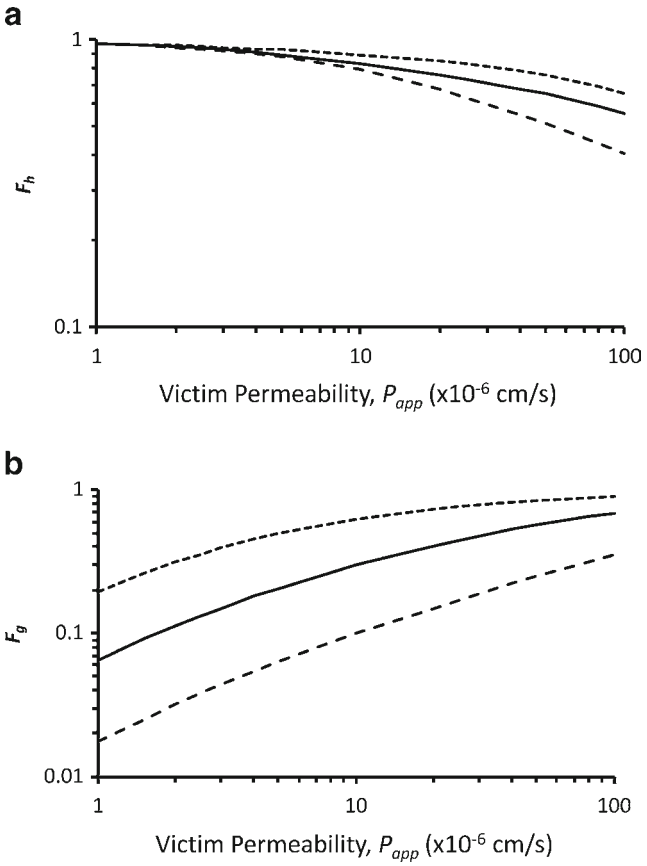

Fig. 8 Computer simulation demonstrating the effect of a 4-fold increase (*long dashed line*) and a 4-fold decrease (*short dashed line*) in CLu_{int} on F_h (**a**) and F_g (**b**). Simulations performed using the best fitting model assuming CYP3A enzyme density increases linearly along the crypt–villous axis. The curves can shift either to the right or left depending on the surface areas are used in the calculations.

existing models, which do take into account area for absorption through the use of P_{eff}, but do not account for the fact that reduced absorption surface area must also lead to reduced volume of enterocyte compartment involved in absorption.

The model was developed using midazolam as a tool compound and simultaneously predicts the time course of midazolam blood concentrations and intestinal bioavailability. The intrinsic clearance per unit CYP3A enzyme estimated in the current study (2.8 μL/min/pmol) is in range with *in vitro* hepatic intrinsic clearance of 1.7–3.8 μL/min/pmol and *in vitro* intestinal intrinsic clearance of 3.0–6.8 μL/min/pmol reported previously(6,27,28). The permeability estimated from the current best fitting model (50.7×10^{-6} cm/s) also compares very well with measured *in vitro* values: 20.3 to 28.5×10^{-6} cm/s (29), 37.9 to 61.1×10^{-6} cm/s (30), 56.4 to 70×10^{-6} cm/s (31). In fact, model predicted midazolam blood concentration and intestinal availability using *in vitro* values for permeability and intrinsic clearance from the literature were in reasonable agreement with experimental data (Fig. 3). The ability to better predict human pharmacokinetics using only *in vitro* and *in silico* data enables better prediction of effective human dose and safety margins earlier in the drug discovery/development process, thus reducing attrition.

The present model also predicted that the effective intestinal surface area for midazolam absorption is approximately 10 times that of the smooth luminal surface area. Compared to the theoretical upper limit of a 30-fold surface area amplification by plicae circulars and villi, this implies that 1/3 of the villous surface is accessible for midazolam absorption (surface accessibility of 0.33). This is very similar to the theoretical accessibility of 0.36 calculated for midazolam using equations derived by Oliver *et al.* (13) at the best fitting permeability of 50.7×10^{-6} cm/s and independently confirms that most if not all absorption of fluid, nutrients and highly permeable drugs takes place in the upper villous regions (12). Oliver *et al.*'s theoretical analysis (13) is limited to drug in solution. Expansion of the analysis to consider the effect of particle size reduction of poor solubility/high permeability drugs in penetrating into the inter-villous space will aid formulation development.

Available literature data on villous dimensions and density in different segments of the intestine is scarce. The current model uses the same, jejunum-based, values in each of the intestinal segments. Since midazolam is predominantly absorbed in the upper small intestine, the impact of a difference in villous dimensions or density between jejunum and ileum will be minimal. In the future, the model may need to be expanded to account for any such differences to improve predictions for low permeability drugs.

A key element of the present work is that it explicitly takes into account the immediate downstream effect of incomplete accessibility of the villous surface by considering distinct absorbing and non-absorbing enterocyte compartments, associated with the accessible and non-accessible villous surfaces, respectively. Such a distinction provides better estimates for enterocyte intracellular concentrations and intestinal intrinsic clearance. Modeling simulation suggests that in case of highly permeable drugs, not doing so will result in overestimation of intestinal metabolism (Fig. 4b) and underestimation of systemic AUC since the amount of CYP3A involved in intestinal metabolism is overestimated.

Making a distinction between absorbing and non-absorbing enterocyte compartments also has important implications for DDI predictions. As illustrated in Fig. 9, the model predicts that a substantial difference in permeability between victim and perpetrator drugs will result in spatial separation of the two along the length of the intestine. Co-administration of a highly permeable perpetrator with a poorly permeable victim will also result in spatial separation of the drugs along the villous surface (Fig. 9a). Such separations will prevent the perpetrator from exerting its full interaction potential. If the high permeability drug also has slow dissolution, then the spatial separation along the intestinal length will diminish, but the spatial separation along the crypt-villous axis will

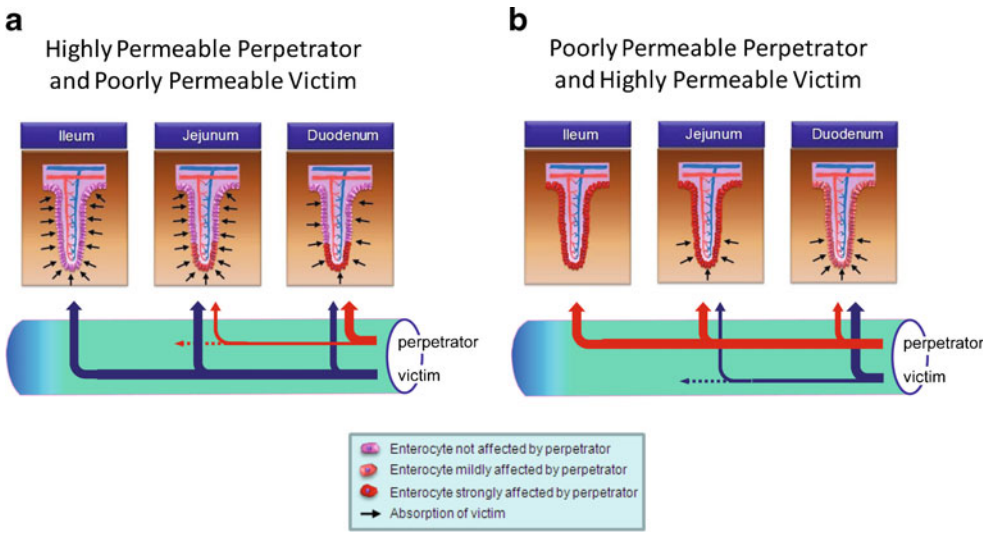

Fig. 9 Spatial separation in the intestine of co-administered drugs with substantial differences in permeability and the consequences for DDIs. A highly permeable drug will be preferentially absorbed in the upper small intestine in the upper regions of the villous. A poorly permeable drug will have greater opportunity to move into the distal parts of the intestine and into the inter-villous space. (**a**) A highly permeable perpetrator will be separated from a poorly permeable victim both along the villous axis and along the intestinal length and therefore will not exert it's full interaction potential on a poorly permeable victim. (**b**) On the contrary, a poorly permeable perpetrator will affect the CYP3A enzymes along most of the villous axis including the tip region where a highly permeable victim is absorbed. It will only be separated from a highly permeable victim along the length of the intestine length.

remain. In case of co-administration of a poorly permeable perpetrator with a highly permeable victim, while both victim and perpetrator will be present at villous tips, they will still be separated spatially along the intestinal length, with the highest victim intracellular enterocyte concentrations reached proximal to the highest perpetrator intracellular concentrations (Fig. 9b). The potential impact of physical separation between victim and perpetrator drugs can now be investigated in future mechanistic PBPK models.

An important aspect of the current model is the presence of permeability-limited enterocyte and liver compartments. On the surface this appears to contradict with the conventional classification of midazolam as highly permeable. However, this apparent contradiction can be understood when the permeability clearance is compared to blood flow in the two tissues. For liver, the permeability clearance calculated based on parameters used in this model is only approximately 10-fold above the typical hepatic blood flow of 92.4 L/hr. Even if the hepatocyte sinusoidal surface area used in the present model underestimates the true value by several fold, the permeability clearance by the liver is still well below 10,000 times the hepatic blood flow, a criterion for using a flow-limited model (9). The margin is even narrower for enterocytes, with an estimated permeability clearance only approximately 2-fold higher than the enterocyte blood flow of 18 L/hr. These calculations suggest that even for compounds classified as highly permeable, the disposition kinetics in enterocytes and hepatocytes can be appropriately modeled according to permeability-limited kinetics. The fact that the predicted F_g and F_h (Fig. 8a and b) are sensitive to permeability between 10 and 100×10^{-6} cm/s further demonstrates the role permeability-limitation plays in drug kinetics in intestine and liver. We have not considered permeability limitation in other tissues. Since other tissues do not participate in drug clearance, this would not affect the model predicted systemic clearance, blood AUC, F_g, or F_h. However, this could affect the terminal half-life and will primarily affect later time points.

Permeability-limitation has several important implications for the kinetics in liver and intestine. As mentioned previously, while high permeability enhances hepatic metabolism, low permeability enhances intestinal metabolism. Consequently, when a compound with very high permeability (> midazolam) is dosed orally it will be subjected to significant hepatic first-pass extraction without significant contribution from the intestine. On the other hand, for compounds with very low permeability, intestine, not liver is the dominating contributor to first-pass extraction. For many compounds in between, including midazolam, both liver and intestine contribute to first-pass extraction.

Permeability not only dictates whether intestine or liver is the predominant contributor to first-pass extraction, it also determines to what extent variation in intrinsic clearance due to induction, inhibition or polymorphism, impacts metabolism in these tissues. Recall from Fig. 8 that, for victim drugs with relatively low permeability (*e.g.* 5×10^{-6} cm/s, for a drug with relatively high CLu_{int}), changes in intrinsic clearance have very little impact on hepatic metabolism (F_h), but a significant effect on intestinal metabolism (F_g). Since intestinal metabolism

contributes primarily to first-pass extraction, but not systemic clearance, a preferential change in intestinal metabolism would result in a change in AUC and Cmax without notable effect on half-life (Fig. 10a). Conversely, for a victim drug with permeability in the range where both liver and intestine contributes to first-pass extraction (*e.g.* 50×10^{-6} cm/s, for a drug with relatively high CLu_{int}) a change in intrinsic clearance has an effect on both F_h and F_g, and consequently notable changes in systemic clearance and half-life (Fig. 10b).

A further dose-dependent effect on CYP3A interaction can be predicted for victim drugs with liver and intestine contributing to first-pass extraction. Since the enterocyte concentration is much higher than the hepatocyte concentration, CYP3A perpetrators could reach an effective enterocyte concentration to impact intestinal CYP3A at much lower doses than required to impact hepatic CYP3A. In this case, a CYP3A perpetrator could preferentially impact intestinal first-pass extraction at low doses, resulting primarily in changes in AUC and Cmax without an obvious effect on half-life, while impacting both intestinal and hepatic first-pass extraction at high doses, resulting in changes in AUC, Cmax as well as half-life.

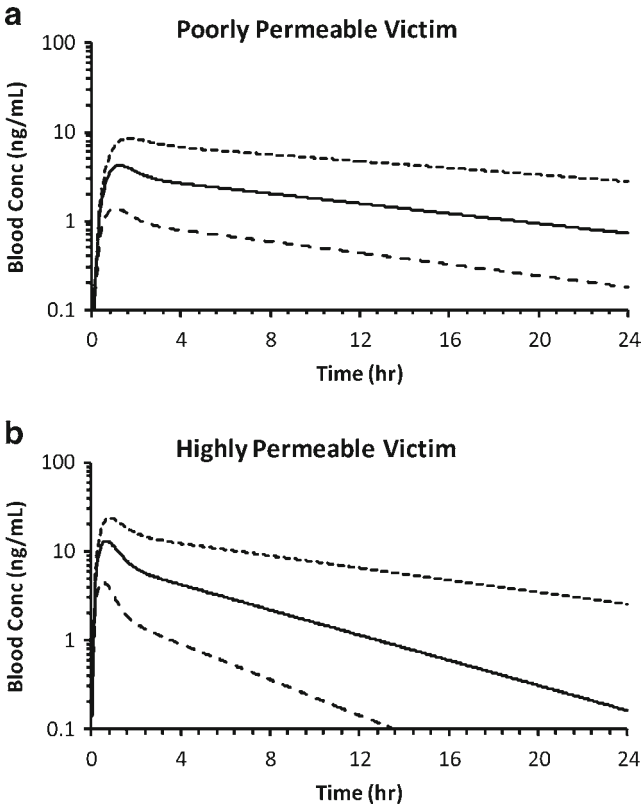

Fig. 10 Computer simulation demonstrating the effect of a 4-fold increase (*long dashed line*) and a 4-fold decrease (short dashed line) in CLu_{int} on the blood concentration time course of poorly permeable (5×10^{-6} cm/s) and highly permeable (50×10^{-6} cm/s) drugs (**a**, **b**). First pass extraction of poorly permeable drugs occurs primarily in the intestine, hence changes in intrinsic clearance result in changes in Cmax and AUC, without a notable effect on half life. First pass extraction of highly permeable drugs, in the range where both liver and intestine contribute to first pass extraction, a change in intrinsic clearance will result in an effect on Cmax, AUC and half life.

The current model, developed for intestinal CYP3A metabolism using midazolam as tool compound, provides a framework that can be readily expanded to incorporate model elements for CYP3A inhibition (32) and induction (33). Because many CYP3A substrates are also substrates of P-glycoprotein, a model which can more realistically consider passive permeability, efflux transport and metabolism can also be used to further query CYP3A-P-gp interplay. Measurement of cell and tissue efflux transporter levels (34), as well as appropriate treatment of efflux transporter kinetics is a very active area of investigation (35–39).

Furthermore, the distinction between absorbing and non-absorbing enterocyte compartments provides a framework for incorporation of morphological and physiological variations along the crypt-villous axis. Enterocytes are formed in intestinal crypts and migrate up the villous as they mature. This results in marked variation in functional and physiological properties along the crypt-villous axis, which can potentially impact intestinal drug absorption and metabolism. The existence of a CYP3A gradient along this axis has already been considered in the present study. Other differences along this axis may be the density of the capillary bed (18), permeability characteristics (40), physical properties of the microvillous membrane (41) or non-uniform distribution of P-glycoprotein efflux transporters (42). Interestingly, the three different CYP3A distribution patterns considered in this study yielded similar fits and best fitting parameters, indicating that CYP3A distribution along the crypt-villous axes does not significantly impact intestinal metabolism for midazolam. Additional analysis using other drugs is needed to evaluate the functional significance of the variation of CYP3A and other properties (*e.g.* transporters) along the crypt-villous axis.

Further work is also required to determine if the current model (or an expanded version) will improve prediction of human PK from *in vitro* data for other compounds as well. Nonetheless, it is anticipated that insights gained from this model will be applicable to other drugs or drug candidates and that more realistic PBPK models will enhance predictions of human pharmacokinetics and DDIs.

REFERENCES

1. Wienkers LC, Heath TG. Predicting in vivo drug interactions from in vitro drug discovery data. Nat Rev Drug Discov. 2005;4:825–33.
2. Peters SA, Schroeder PE, Giri N, Dolgos H. Evaluation of the use of static and dynamic models to predict drug-drug interaction and its associated variability: impact on drug discovery and early development. Drug Metab Dispos. 2012;40:1495–507.
3. Einolf HJ. Comparison of different approaches to predict metabolic drug-drug interactions. Xenobiotica. 2007;37:1257–94.

4. Paine MF, Khalighi M, Fisher JM, Shen DD, Kunze KL, Marsh CL, *et al.* Characterization of interintestinal and intraintestinal variations in human CYP3A-dependent metabolism. J Pharmacol Exp Ther. 1997;283:1552–62.
5. Yang J, Tucker GT, Rostami-Hodjegan A. Cytochrome P450 3A expression and activity in the human small intestine. Clin Pharmacol Ther. 2004;76:391.
6. Paine MF, Shen DD, Kunze KL, Perkins JD, Marsh CL, McVicar JP, *et al.* First-pass metabolism of midazolam by the human intestine. Clin Pharmacol Ther. 1996;60:14–24.
7. Yang J, Jamei M, Yeo KR, Tucker GT, Rostami-Hodjegan A. Prediction of intestinal first-pass drug metabolism. Curr Drug Metab. 2007;8:676–84.
8. Cong D, Doherty M, Pang KS. A new physiologically based, segregated-flow model to explain route-dependent intestinal metabolism. Drug Metab Dispos. 2000;28:224–35.
9. Gertz M, Houston JB, Galetin A. Physiologically based pharmacokinetic modeling of intestinal first-pass metabolism of CYP3A substrates with high intestinal extraction. Drug Metab Dispos. 2011;39:1633–42.
10. Tam D, Tirona RG, Pang KS. Segmental intestinal transporters and metabolic enzymes on intestinal drug absorption. Drug Metab Dispos. 2003;31:373–83.
11. Lennernas H. Human intestinal permeability. J Pharm Sci. 1998;87:403–10.
12. Pappenheimer JR, Michel CC. Role of villus microcirculation in intestinal absorption of glucose: coupling of epithelial with endothelial transport. J Physiol. 2003;553:561–74.
13. Oliver RE, Jones AF, Rowland M. What surface of the intestinal epithelium is effectively available to permeating drugs? J Pharm Sci. 1998;87:634–9.
14. Cubitt HE, Yeo KR, Howgate EM, Rostami-Hodjegan A, Barter ZE. Sources of interindividual variability in IVIVE of clearance: an investigation into the prediction of benzodiazepine clearance using a mechanistic population-based pharmacokinetic model. Xenobiotica. 2011;41:623–38.
15. Thummel KE, O'Shea D, Paine MF, Shen DD, Kunze KL, Perkins JD, *et al.* Oral first-pass elimination of midazolam involves both gastrointestinal and hepatic CYP3A-mediated metabolism. Clin Pharmacol Ther. 1996;59:491–502.
16. DeSesso JM, Jacobson CF. Anatomical and physiological parameters affecting gastrointestinal absorption in humans and rats. Food Chem Toxicol. 2001;39:209–28.
17. Krogh A. The progress of physiology. Science. 1929;70:200–4.
18. Casley-Smith JR, O'Donoghue PJ, Crocker KW. The quantitative relationships between fenestrae in jejunal capillaries and connective tissue channels: proof of "tunnel-capillaries". Microvasc Res. 1975;9:78–100.
19. Buddington RK, Diamond JM. Ontogenetic development of intestinal nutrient transporters. Annu Rev Physiol. 1989;51:601–19.
20. Blouin A, Bolender RP, Weibel ER. Distribution of organelles and membranes between hepatocytes and nonhepatocytes in the rat liver parenchyma. A stereological study. J Cell Biol. 1977;72:441–55.
21. Keppler D, Arias IM. Hepatic canalicular membrane. Introduction: transport across the hepatocyte canalicular membrane. FASEB J. 1997;11:15–8.
22. Strocchi A, Levitt MD. Role of villous surface area in absorption. Science versus religion. Dig Dis Sci. 1993;38:385–7.
23. Backman JT, Kivisto KT, Olkkola KT, Neuvonen PJ. The area under the plasma concentration-time curve for oral midazolam is 400-fold larger during treatment with itraconazole than with rifampicin. Eur J Clin Pharmacol. 1998;54:53–8.
24. Kupferschmidt HH, Ha HR, Ziegler WH, Meier PJ, Krahenbuhl S. Interaction between grapefruit juice and midazolam in humans. Clin Pharmacol Ther. 1995;58:20–8.
25. Palkama VJ, Ahonen J, Neuvonen PJ, Olkkola KT. Effect of saquinavir on the pharmacokinetics and pharmacodynamics of oral and intravenous midazolam. Clin Pharmacol Ther. 1999;66:33–9.
26. Saari TI, Laine K, Leino K, Valtonen M, Neuvonen PJ, Olkkola KT. Effect of voriconazole on the pharmacokinetics and pharmacodynamics of intravenous and oral midazolam. Clin Pharmacol Ther. 2006;79:362–70.
27. Gertz M, Harrison A, Houston JB, Galetin A. Prediction of human intestinal first-pass metabolism of 25 CYP3A substrates from in vitro clearance and permeability data. Drug Metab Dispos. 2010;38:1147–58.
28. Obach RS. Prediction of human clearance of twenty-nine drugs from hepatic microsomal intrinsic clearance data: an examination of in Vitro half-life approach and nonspecific binding to microsomes. Drug Metab Dispos. 1999;27:1350–9.
29. Fisher JM, Wrighton SA, Watkins PB, Schmiedlin-Ren P, Calamia JC, Shen DD, *et al.* First-pass midazolam metabolism catalyzed by 1alpha,25-dihydroxy vitamin D3-modified Caco-2 cell monolayers. J Pharmacol Exp Ther. 1999;289:1134–42.
30. Tolle-Sander S, Rautio J, Wring S, Polli JW, Polli JE. Midazolam exhibits characteristics of a highly permeable P-glycoprotein substrate. Pharm Res. 2003;20:757–64.
31. Polli JW, Wring SA, Humphreys JE, Huang L, Morgan JB, Webster LO, *et al.* Rational use of in vitro P-glycoprotein assays in drug discovery. J Pharmacol Exp Ther. 2001;299:620–8.
32. Obach RS, Baxter JG, Liston TE, Silber BM, Jones BC, MacIntyre F, *et al.* The prediction of human pharmacokinetic parameters from preclinical and in vitro metabolism data. J Pharmacol Exp Ther. 1997;283:46–58.
33. Chen EP, Chen L, Ji Y, Tai G, Wen YH, Ellens H. A mechanism-based mathematical model of aryl hydrocarbon receptor-mediated CYP1A induction in rats using beta-naphthoflavone as a tool compound. Drug Metab Dispos. 2010;38:2278–85.
34. Tucker TG, Milne AM, Fournel-Gigleux S, Fenner KS, Coughtrie MW. Absolute immunoquantification of the expression of ABC transporters P-glycoprotein, breast cancer resistance protein and multidrug resistance-associated protein 2 in human liver and duodenum. Biochem Pharmacol. 2012;83:279–85.
35. Fan J, Maeng HJ, Pang KS. Interplay of transporters and enzymes in the Caco-2 cell monolayer: I. effect of altered apical secretion. Biopharm Drug Dispos. 2010;31:215–27.
36. Kalvass JC, Pollack GM. Kinetic considerations for the quantitative assessment of efflux activity and inhibition: implications for understanding and predicting the effects of efflux inhibition. Pharm Res. 2007;24:265–76.
37. Lumen AA, Acharya P, Polli JW, Ayrton A, Ellens H, Bentz J. If the KI is defined by the free energy of binding to P-glycoprotein, which kinetic parameters define the IC50 for the Madin-Darby canine kidney II cell line overexpressing human multidrug resistance 1 confluent cell monolayer? Drug Metab Dispos. 2010;38:260–9.
38. Tachibana T, Kato M, Takano J, Sugiyama Y. Predicting drug-drug interactions involving the inhibition of intestinal CYP3A4 and P-glycoprotein. Curr Drug Metab. 2010;11:762–77.
39. Tran TT, Mittal A, Aldinger T, Polli JW, Ayrton A, Ellens H, *et al.* The elementary mass action rate constants of P-gp transport for a confluent monolayer of MDCKII-hMDR1 cells. Biophys J. 2005;88:715–38.
40. Fihn BM, Sjoqvist A, Jodal M. Permeability of the rat small intestinal epithelium along the villus-crypt axis: effects of glucose transport. Gastroenterology. 2000;119:1029–36.
41. Meddings JB, DeSouza D, Goel M, Thiesen S. Glucose transport and microvillus membrane physical properties along the crypt-villus axis of the rabbit. J Clin Invest. 1990;85:1099–107.
42. Meyers MB, Scotto KW, Sirotnak FM. P-glycoprotein content and mediation of vincristine efflux: correlation with the level of differentiation in luminal epithelium of mouse small intestine. Cancer Commun. 1991;3:159–65.

43. Yu LX, Lipka E, Crison JR, Amidon GL. Transport approaches to the biopharmaceutical design of oral drug delivery systems: prediction of intestinal absorption. Adv Drug Deliv Rev. 1996;19(3):359–76.
44. Chaudhuri TK. Use of 99mTc-DTPA for measuring gastric emptying time. J Nucl Med. 1974;15(6):1–5.
45. Fenneteau F, Poulin P, Nekka F. Physiologically based predictions of the impact of inhibition of intestinal and hepatic metabolism on human pharmacokinetics of CYP3A substrates. J Pharm Sci. 2010;99(1):486–514.
46. Brown RP, Delp MD, Rhomberg SL, Beliles RP. Physiological parameter values for physiologically based pharmacokinetic models. Toxicol Ind Health. 1997;13(4):407–84.
47. van Richter O, Burk O, Fromm MF, Thon KP, Eichelbaum M, Kivisto KT. Cytochrome P450 3A4 and P-glycoprotein expression in human small intestinal enterocytes and hepatocytes: a comparative analysis in paired tissue. Clin Pharmacol Ther. 2004;75(3):172–83.
48. Tabbaa MG, Axon ATR, Dixon MF. Enterocyte dimensions in patients with abnormal intestinal permeability. Eur J Gastroenterol Hepatol. 1994;6:607–10.